

On the origin of mixed-layered clay minerals from the San Andreas Fault at 2.5–3 km vertical depth (SAFOD drillhole at Parkfield, California)

A. M. Schleicher · L. N. Warr · B. A. van der Pluijm

Received: 18 January 2008 / Accepted: 11 July 2008 / Published online: 3 August 2008
© Springer-Verlag 2008

Abstract A detailed mineralogical study is presented of the matrix of mudrocks sampled from spot coring at three key locations along the San Andreas Fault Observatory at depth (SAFOD) drill hole. The characteristics of authigenic illite–smectite (I–S) and chlorite–smectite (C–S) mixed-layer mineral clays indicate a deep diagenetic origin. A randomly ordered I–S mineral with ca. 20–25% smectite layers is one of the dominant authigenic clay species across the San Andreas Fault zone (sampled at 3,066 and 3,436 m measured depths/MD), whereas an authigenic illite with ca. 2–5% smectite layers is the dominant phase beneath the fault (sampled at 3,992 m MD). The most smectite-rich mixed-layered assemblage with the highest water content occurs in the actively deforming creep zone at ca. 3,300–3,353 m (true vertical depth of ca. 2.7 km), with I–S (70:30) and C–S (50:50). The matrix of all mudrock samples show extensive quartz and feldspar (both plagioclase and K-feldspar) dissolution associated with the crystallization of pore-filling clay minerals. However, the effect of rock deformation in the matrix appears only minor, with weak flattening fabrics defined largely by kinked and

fractured mica grains. Adopting available kinetic models for the crystallization of I–S in burial sedimentary environments and the current borehole depths and thermal structure, the conditions and timing of I–S growth can be evaluated. Assuming a typical K^+ concentration of 100–200 ppm for sedimentary brines, a present-day geothermal gradient of 35°C/km and a borehole temperature of ca. 112°C for the sampled depths, most of the I–S minerals can be predicted to have formed over the last 4–11 Ma and are probably still in equilibrium with circulating fluids. The exception to this simple burial pattern is the occurrence of the mixed layered phases with higher smectite content than predicted by the burial model. These minerals, which characterize the actively creeping section of the fault and local thin film clay coating on polished brittle slip surfaces, can be explained by the influence of either cooler fluids circulating along this segment of the fault or the flow of K^+ -depleted brines.

Keywords SAFOD · Illite–smectite · Mixed-layered clays · San Andreas Fault

Communicated by T.L. Grove.

A. M. Schleicher (✉)
Geozentrum Nordbayern, Universität Erlangen-Nürnberg,
Schloßgarten 5, 91054 Erlangen, Germany
e-mail: aschleic@umich.edu

L. N. Warr
Institut für Geographie und Geologie,
Ernst-Moritz-Armdt-Universität Greifswald,
Friedrich-Ludwig-Jahn-Str. 17a, 17487 Greifswald, Germany

A. M. Schleicher · B. A. van der Pluijm
Department of Geological Sciences, University of Michigan,
1100 N. University Ave, Ann Arbor, MI 48109, USA

Introduction

The crystallization of clays in fault zones and their influence on fluid–rock interaction, rock deformation and shear strength has been suggested as a possible explanation for a weak fault behavior (Rutter et al. 1986; Vrolijk and van der Pluijm 1999; Rutter et al. 2001; Warr and Cox 2001). As often reported along exhumed segments of the San Andreas Fault in western California, the occurrence of such mineral phases as chlorite, illite, smectite, as well as kaolinite, serpentine and talc, are typically associated with strong fluid–rock interaction and brittle deformation under low-

temperature conditions (Wu et al. 1974; Evans and Chester 1995; Solum et al. 2003; Moore and Rymer 2007). Whereas the San Andreas Fault is probably the most intensively studied fault zone in the world, investigations have mostly been restricted to exposed rocks, where alterations during exhumation are difficult to distinguish from those occurring at depth. In contrast, rock material from drill cores is generally well preserved and lacks the effects of recent surface alteration.

The San Andreas Fault Observatory at Depth (SAFOD) drill hole provides a unique opportunity to characterize the natural state of clay minerals in variably sheared mudrocks at depth, and to directly investigate their alteration where faulting takes place. Previous studies of rock cuttings from the pilot and the main borehole revealed a diverse assemblage of clay mineral phases in various segments of the fault zone. The occurrence of illite, illite–smectite (I–S), chlorite, chlorite–smectite (C–S), and occasional talc and serpentine fragments (Solum and van der Pluijm 2005; Solum et al. 2006; Schleicher et al. 2006; Bradbury et al. 2007; Moore and Rymer 2007) is well documented. Several studies suggested that the occurrence of swelling clays in such mudrocks, either in discrete form or as mixed-layered clay minerals can significantly influence the mechanical properties of fault zones. From laboratory experiments it is known that hydrous smectite minerals lower the shear strength of sedimentary rocks and therefore the presence of interlayer water is a possible cause of fault weakness (Bird 1984; Saffer and Marone 2003; Tembe et al. 2006; Morrow et al. 2007; Ikari et al. 2007).

An important part of the challenge to link mineral growth, fault behavior and the circulation of crustal fluids in sedimentary rocks is to have thorough knowledge of the diagenetic history in space and time. In sedimentary basins many clay minerals develop as a consequence of relatively slow burial over many millions of years, whereas they can form significantly faster during faulting processes. The study of I–S minerals has helped to resolve the geological history of clay crystallization and fluid–rock interaction in numerous rock sequences and has become an important tool for evaluating the burial and thermal history throughout the geological record (Srodon et al. 1986; Hansen and Lindgreen 1989; Lanson and Champion 1991; Nieto et al. 1996; Dong et al. 1997). In the SAFOD samples, the investigation of illite and I–S minerals, and its comparison with faulting and diagenesis history is of particular importance, as such clay minerals are perhaps the best understood in terms of their conditions of formation in buried sedimentary rocks.

In this study, we highlight the nature of mixed-layered clay minerals within mineralized mudrocks sampled from three key locations in the San Andreas Fault, which were cored during the SAFOD activities in summers 2004 and

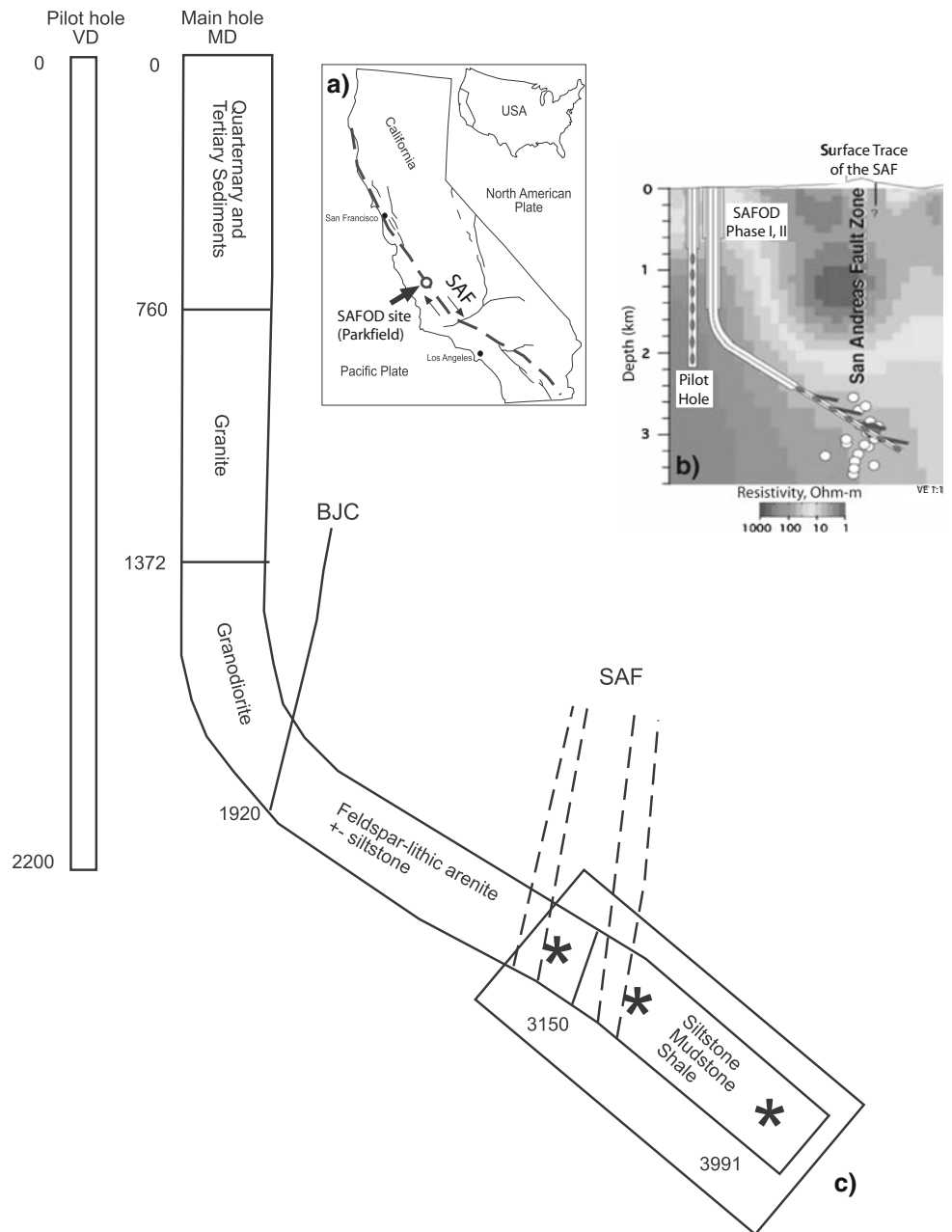
2005. Based on a detailed characterization of the composition, structure and fabric of authigenic mixed-layer clays by X-ray diffraction (XRD) and high resolution electron microscopy (HRTEM), the reaction products are evaluated using the kinetic model of Huang et al. (1993), in combination with the available borehole constraints. Here we propose that most, but not all of the I–S minerals are of late diagenetic origin and crystallized slowly over the last 4–11 Ma of prograde burial history. The localized and probably more rapid precipitation of clays with higher smectite-content within the creeping segment of the fault is a prime candidate to explain the mechanically weak behavior of the San Andreas Fault at Parkfield.

The SAFOD project

The San Andreas Fault is the boundary between the northwestward moving western Pacific Plate and the eastern North American Plate (Fig. 1a). This more than 1,200 km long, dextral strike-slip fault extends to a depth of at least 15 km into the crust and is marked by a complex network of crushed and fractured rocks in a zone from a few hundred meters to kilometers wide (e.g., Wallace 1990). The SAFOD (San Andreas Fault Observatory at Depth) drill site is located ca. 9 km NW of Parkfield/California and lies in a complex area of contractional, extensional and strike-slip deformation with the Salinian granitic block in the west and the Franciscan block to the east (Dickinson 1966; Page et al. 1998; Bradbury et al. 2007). The fault appears at the surface about 1.8 km east of the drill site, and is moving through a combination of earthquakes and fault creep. It is characterized by numerous micro-earthquakes (M_w 0–2) that nucleate at relatively shallow depths of 2–3 km (Nadeau et al. 2004). As part of the Earthscope initiative (<http://www.icdp-online.de/sites/sanandreas/index/>) the aim of the SAFOD project is to sample and instrument the San Andreas Fault at depth, in order to address fundamental questions regarding earthquake and fault mechanics (Hickman et al. 2004; Fig. 1b). The primary objectives of the drilling activity are to assess the structure and composition of the active San Andreas Fault where micro-earthquakes nucleate, and to determine the interplay between rock formation, faulting, heat flow and fluid migration in an active member of the fault system (Thurber et al. 2004; Williams et al. 2004; Solum and van der Pluijm 2005; Boness and Zoback 2006).

In 2002, a vertical pilot hole was drilled through quartz pebbly sandstone into the Salinian granite to a depth of 2.2 km (Hickman et al. 2004). The main hole, drilled during 2004 (Phase 1) and 2005 (Phase 2) is vertical to a depth of approximately 1,700 m, where it deviates with an angle of approximately 55° in order to intersect the trace of the San Andreas Fault at around 2,700 m true

Fig. 1 **a** Location map of the SAFOD drillhole in Parkfield/California, **b** Sketch of the SAFOD drilling directions of the Pilot hole and the Main hole, **c** depth profiles of the borehole with different rock lithologies drilled during Phase 1 and Phase 2 in summers of 2004 and 2005, modified after Dong et al. (1997). Sample-set 1: 10,062 ft (3,066 m), run B0022/23, Section R0005, sample-set 2: core catcher drilled during summer 2005, sample-set 3: 13,097 ft (3,992 m), box 3, run B0003, Section R0005



vertical depth/TVD (Fig. 1b). Phase 1 drilling was completed in 2004, with drilling through Quaternary and Tertiary sediments, granite/granodiorite and into arkosic sediments (Hickman et al. 2005). Phase 2 activities completed drilling to 3,992 m measured depth/MD. This drilling extended into interbedded mudstone, siltstone and shale lithologies at the bottom of the hole. In summer 2007, Phase 3 provided approximately 40 m of cores by drilling through specific sections of the fault.

Based on petrologic and mineralogic observations of SAFOD rock cuttings, a complex geology characterized by a number of fault zones has been detected (Draper et al. 2005; Solum et al. 2006; Bradbury et al. 2007; Fig. 1c). The

lithologies cored through the San Andreas main fault consist mainly of sandstones, siltstones and shaly mudstones with some serpentinite clasts. Microfossil observations (K. Mc Dougall, written communication in Bradbury et al. 2007), and the occurrence of volcanic quartz and detrital olivine grains suggest these rocks belong to the Cretaceous uppermost Great Valley sequence.

Sample material and analytical methods

Rock fragments from three spot cores at different depths were sampled (Fig. 1c; Table 1). The rocks from sample-

Table 1 List of the data used in this study determined by X-ray diffraction analysis and electron microscopy for the three studied mudrock samples

Sample (MD)	Sample (TVD)	Fabric intensity (m.r.d.)	Whole rock minerals	Fine-grained fraction	% Sm in I–S	Total water loss % (TGA–DTA)	Max. paleo-temperature (I–S) (°C)
3,066 m	2,480 m	2.0–2.7	qtz, pl, kfs, mica	Il, I–S	20.0	3.66 (0.7 IW)	170
3,436 m	2,696 m	2.06–2.4	qtz, pl, kfs, mica	Il, I–S, sm, chl, C–S, lmt	25.0	6.5 (2.96 IW)	110
3,992 m	3,014 m	1.9–2.1	qtz, pl, kfs, mica	Il, chl	max 5.0	2.75 (0 IW)	~200

MD measured depth, TVD true vertical depth, qtz quartz, pl plagioclase (albite, anorthite), kfs K-feldspar, mica muscovite, biotite, I–S illite-smectite, C–S chlorite–smectite, sm smectite, lmt laumontite, IW interlayer water

set 1 derive from a ~30-cm broad, clay-rich shear zone at 3,065.9–3,066.9 m MD, positioned in the lowest part of fine-grained arkosic and lithic arenite containing siltstones and mudstones (Bradbury et al. 2007). This zone belongs to a fault zone drilled during Phase 1 in summer 2004. It appears ca. 300 m above the main fault and is characterized by recent casing deformation (Zoback et al. 2005). The second group of rock fragments (sample-set 2) comes from ca. 3,436 m MD, where interbedded mudstone, siltstone and shaly rock chips up to 60 mm in size were recovered in a core catcher. These samples belong to the main fault at 3,300–3,353 m MD, which is marked by an area of intense fracturing, casing deformation at ca. 3,300 m (Zoback et al. 2005) and enhanced cataclasis combined with strong alteration (Bradbury et al. 2007). The third spot-core, drilled during Phase 2 in the summer of 2005, represents clay-rich siltstones from the deepest part of the drillhole at 3,991.3–3,992.3 m MD (sample-set 3; from here on, the sample depths indicate measured depth/MD unless mentioned differently). Whereas sample-set 2 and 3 belong geologically to the Great Valley sequence (Bradbury et al. 2007), sample-set 1 lies in the transition zone between the Tertiary arkosic sediments and the Great Valley sequence. Based on the diagenetic characteristics of the I–S investigated, we assume these sheared mudrocks to be part of the Great Valley sequence.

Electron microscopy and X-ray texture goniometry (XTG) investigations were undertaken at the University of Michigan (EMAL: Electron Microbeam Analysis Laboratory). Samples were first examined by secondary and back-scattered scanning electron microscopy (SEM) using carbon-coated rock fragments and polished thin sections. Semiquantitative analysis of the mineral composition was obtained by energy-dispersive spectroscopy (EDS). Key spots were analyzed by high-resolution transmission electron microscopy (HRTEM) and analytical electron microscopy (AEM) techniques following the analytical procedures outlined by Peacor (1992) and Warr and Nieto (1998). Samples were vacuum impregnated with L.R. white resin following the procedure of Kim et al. (1995) to prevent the collapse of smectite interlayers. Small washers

(1 mm in diameter) were glued onto the key spots, ion milled and then carbon coated before investigation. The TEM used was a Phillips CM 12 scanning-transmission electron microscope (STEM) with a KeveX Quantum solid-state detector. It operates at 120 kV and 20 mA. The EDS-AEM data were obtained in scanning transmission electron mode using a beam diameter of 5 nm and a scanning area of 30 × 30 nm. Compositional data were calibrated using the *k* values obtained from analyses of available laboratory standards.

Thermogravimetric analysis (TGA) combined with differential thermal analysis (DTA) was carried out on whole-rock samples at the IPCMS of the Université Louis Pasteur of Strasbourg (ULP), in France. The method consists of heating a small amount of powdered sample at a constant rate up to 1,100°C and recording the relative weight and temperature changes that take place in the material during heating (Grim and Rowland 1944). This method provides information about mineralogy, water content and water storage sites in the minerals.

Thick rock sections (~200–400 μm) of selected samples were prepared for determining the crystallographic-preferred orientation of phyllosilicates by XTG (e.g., Oertel 1985; van der Pluijm et al. 1994; Ho et al. 1999; Day-Stirrat et al. 2008). Analyses were made using an Enraf-Nonius CAD4 automated single-crystal diffractometer with a Mo radiation source, equipped with a custom-built X-ray pole figure stage. The clay phases are identified by an X-ray diffractogram. The detector is moved to the (001) plane of the mineral ($d = 10 \text{ \AA}$ for mica and 10–13 Å for I–S), and the location and intensity of the diffracted beam at ~1,300 different positions collected and plotted in an equal area projection and contoured as multiples of a random distribution (m.r.d.). This is a standard statistical measure of the relative randomness of a distribution (Wenk 1985). Higher values represent a larger degree of mineral preferred orientation. Due to the small sample areas (~1 mm²) used to measure the fabric of the phyllosilicates, better results were obtained by multiple XTG analyses (up to four measurements) and averaging the results (Solum et al. 2003).

For powder XRD analysis, the rock chips were hand-crushed and the clay size fractions (<2 μm) separated. The XRD analysis of the random powder and texture preparation followed the analytical methods described by Moore and Reynolds (1997). Clay minerals were identified and analyzed using a Siemens/Bruker D5000 X-ray diffractometer at the CGS, Université Louis Pasteur in Strasbourg, France. Air-dried and ethylene-glycol solvated oriented mounts were scanned from 2° to 50° at 0.02°2 θ intervals using CuK α radiation produced at 40 kV and 30 mA. Measurements of XRD peak heights, areas, and peak widths were made using the Siemens Diffrac-AT software. Smectite and I–S determination was based on comparisons between air dried and ethylene-glycol treated texture samples. The percentage of smectite in I–S was identified by matching the measured XRD patterns against calculated profiles using the program NEWMOD (Reynolds and Reynolds 1996). These calculated XRD patterns were produced by varying the abundance of the mixed layer components, the particle (crystallite) thickness and the degree of ordering (Reichweite). Illite polytype identification was based on the diffraction criteria of Moore and Reynolds (1997), using relative intensities at 3.07, and 3.66 Å for the 1M and 3.88, 3.72, 3.49, 3.2, 2.98, and 2.86 Å for the 2M₁ polytype, respectively.

Results

Mineralogy and texture

The main mineral assemblages of all sample sets investigated contain clasts of quartz, feldspar (plagioclase and K-feldspar) and mica (mostly biotite), set in a fine-grained matrix (Table 1). Each sample set shows signs of strong rock alteration, in particular intense dissolution of clasts and chloritization of mafic components. Based on back-scattered and secondary electron SEM imaging (Fig. 2a, c, e), the detrital biotite generally ranges up to 300 μm in basal length and shows a variety of deformation and alteration states. The XTG results reveal weak fabrics of the mica grains in all mudrocks with the basal orientation (001) ranging from m.r.d. 1.9–2.7 (Fig. 2b, d, f; Table 1). At 3,066 m, the grains show distinct kinking and the highest degree of preferred orientation with an average m.r.d. of 2.4 (2.0–2.7 Fig. 2a, b, Table 1). The range of values probably reflects the combined influence of the fine-grained authigenic I–S minerals and the presence of coarser, detrital mica grains of varying deformation states. However, the latter appear to be the more important controlling feature due to the better crystallinity of these fabric elements. The elongated pyrite crystals that grow in the big detrital micas indicate their crystallization with sulfide-

bearing fluids under reducing conditions (Pares et al. 2008; Fig. 2a). At 3,436 m, the micas are more fractured and show more distinct dissolution features caused by intense fluid–rock interaction. The fracturing and shorter average lengths (ca. 100 μm) of these detrital micas is probably responsible for the poorer preferred orientation than found in sample set 1, with an average m.r.d. of 2.2 (2.06–2.4, Fig. 2b, c; Table 1). At 3,992 m, no intense fracturing or deformation is recognizable with only slightly curved grains (Fig. 2e). The poorly developed XTG fabric of this sample, with an average m.r.d. value of 2.0 (1.9–2.1, Fig. 2f; Table 1) may result from the coarser growth of authigenic material within pore space, or due to the weaker alignment of detrital mica grains (Fig. 2f).

Clay mineralogy

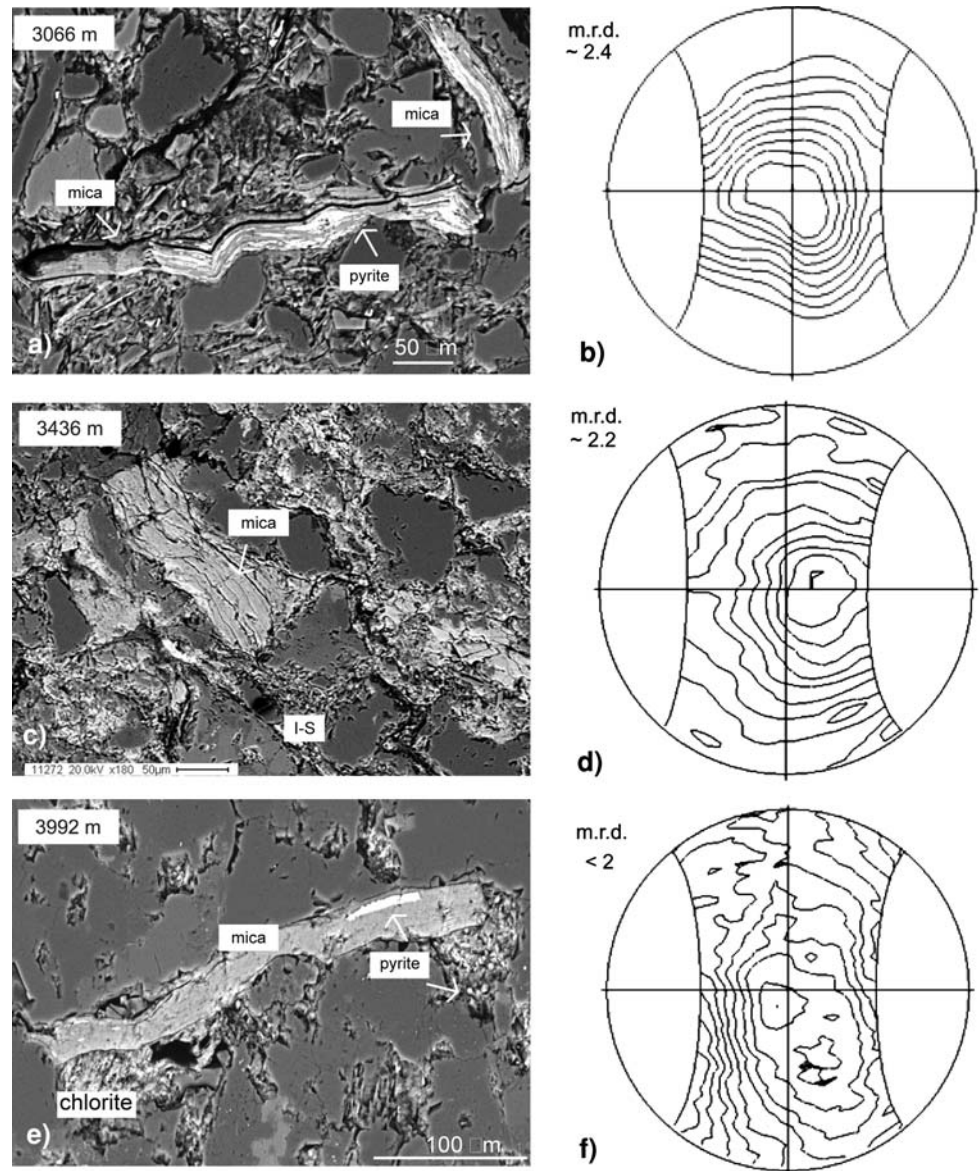
The whole rock and the fine grained (<2 μm) mineral assemblages of the three sample-sets show variable amounts of clay minerals that are summarized in Fig. 3a and Table 1 (from Solum et al. 2006 and this study). The very fine grained and dark gray to black shaly rock fragments at 3,066 m are estimated to be composed of 62–69 weight % (wt%) clay (48–51 wt% illite and 14–18 wt% I–S), with additional alteration phases of chlorite, calcite and zeolite (Fig. 3a; Solum et al. 2006). These samples contain numerous polished fracture surfaces with striations and thin film clay coatings that are characteristic of fault rocks (Schleicher et al. 2006).

The silty mudstones at 3,436 m are fine-grained, quartz- and feldspar- (both plagioclase and K-feldspar) rich with numerous polished fracture surfaces and distinct striations. The rocks are fractured with very thin sets of veins that are filled with calcite and some discrete smectite. The clay content in this area ranges between 14 and 60 wt% and is basically composed of chlorite, illite, I–S and C–S, with additional ~6 wt% calcite (mostly as vein fillings) and <1 wt% laumontite and serpentine in pores (Solum et al. 2006).

The shaly samples at 3,991 m show small calcite-filled veins, and less polished surfaces. The rock chips are very fine-grained, with chlorite, illite, fine-grained calcite, laumontite and pyrite. The main mineral components are quartz, albite/anorthite, K-feldspar, biotite, muscovite and chlorite.

SEM imaging of the rock fragments show at least two types of illitic minerals in different amounts within all spot cores (Fig. 3b–d). The fine-grained crystals are largely authigenic I–S with less than ~2 μm basal length and pseudohexagonal to flaky shapes. They occur mostly within pores or along fractures and veins. A coarser-grained, detrital illite with pseudohexagonal shapes ranges between 2–10 μm in basal length. These grains show

Fig. 2 SEM and XTG analysis of mica grains (muscovite, biotite, chlorite) of the three mudrock sample-sets investigated. **a** and **b** are of the sample at 3,066 m which contain slightly bent and fractured mica grains (mostly biotite), and an average fabric (up to four measurements) with a m.r.d. value of 2.4. **c** and **d** show the intensity of fracturing and folding is highest at 3,436 m, with a slightly weaker fabric and smaller m.r.d. value of 2.2. **e** and **f** the clay-rich lithologies at 3,992 m lying beneath the fault show mostly intact rock clasts, and an XTG pattern characteristic of very weak compaction (m.r.d. <2). Pole figures have been rotated so that the center of the distribution is in the center of the plot

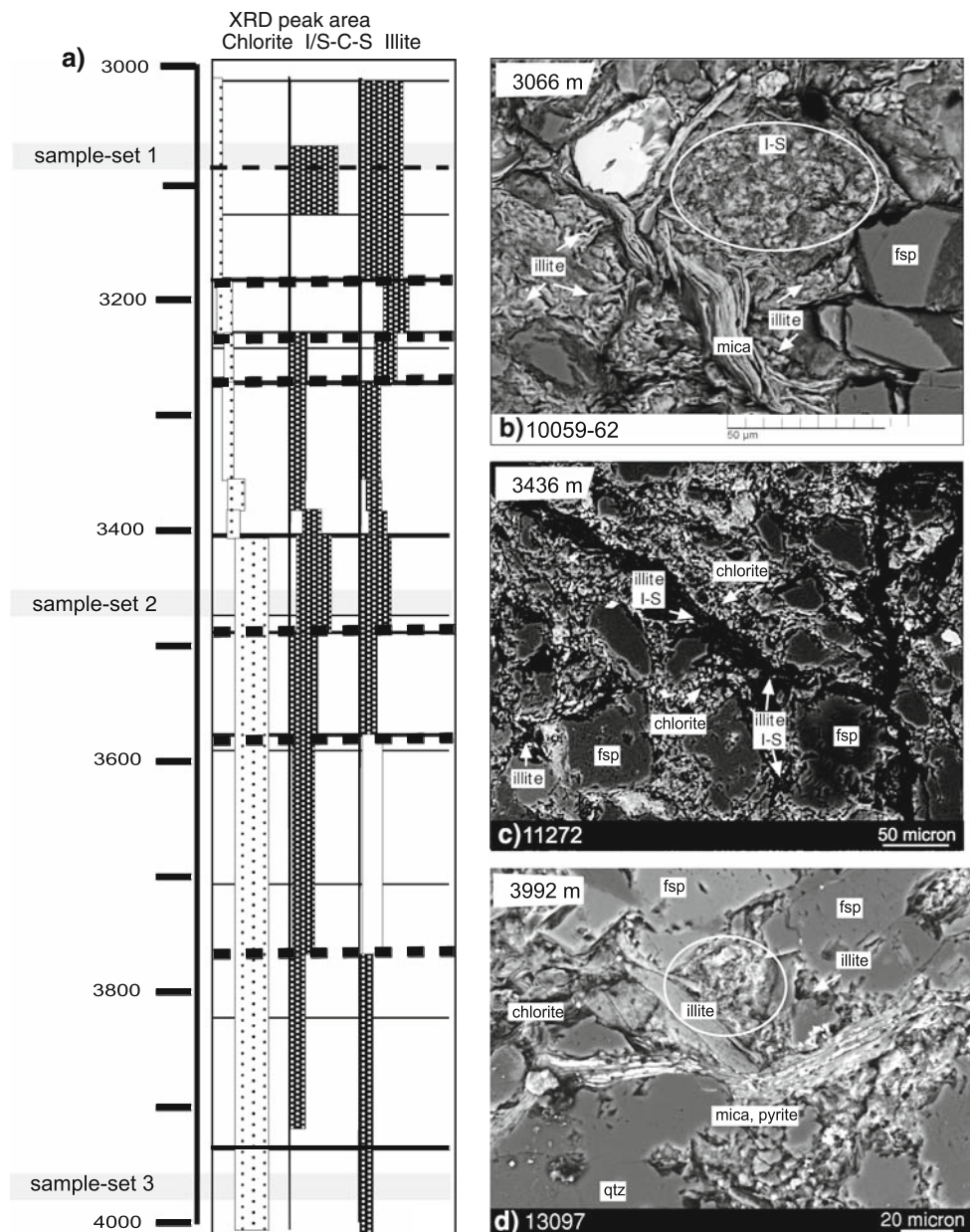


characteristic signs of particle dissolution with irregular and sutured crystal edges. At 3,066 m, fine-grained I-S occurs mainly as pore-filling phases (Fig. 3b), whereas at 3,436 m, I-S is additionally located in fractures and some mineralized veinlets, sometimes as thin platelets together with coarser grained illite or chlorite (Fig. 3c). At 3,992 m, chlorite minerals clearly dominate, but some coarse-grained illite have grown most likely as an alteration product of larger biotite-chlorite flakes and K-feldspar (Fig. 3d). The finer grained authigenic I-S type has not been recognized by SEM in this sample-set.

The random XRD powder diffractograms for polytype determination confirm the mixture of at least two different types of illitic minerals (Fig. 4). At 3,066 m, the specific XRD peaks between 19° and $36^\circ 2\theta$ indicate the presence of an authigenic 1 M polytype in the smallest grain size

fraction (Fig. 4a; Moore and Reynolds 1997). A broad reflection hump and a raised background level indicate a high degree of disordering (a $1M_d$ polytype). In the larger grain sizes ($>2 \mu\text{m}$), a $2M_1$ polytype occurs, reflecting the illite of detrital origin (Moore and Reynolds 1997). The intensity of these diagnostic reflections show consistent variations with grain size, whereby the 1-M polytype peaks slightly increase toward finer grain sizes and the $2M_1$ reflections progressively decrease. These trends are apparent in the illite-rich samples at 3,066 m, but are more difficult to resolve in the deeper samples (3,992 m, 3,436 m; Fig. 4b) due to the overlap of feldspar reflections or to the lack of sample material. However, in all sample sets investigated, mixtures of authigenic 1 M and detrital $2M_1$ polytypes can be recognized by combined SEM and XRD study.

Fig. 3 **a** Mineralogical profile, modified after Solum et al. (2006), showing the variations in clay mineral assemblages through the deeper section of the drillhole between 3,000 and 4,000 m with mixtures of chlorite, illite and mixed-layered I–S and C–S, **b–d** SEM images showing illite and I–S grains of different shape and size within the three sample-sets investigated



Microstructure and chemistry of I–S and illite minerals

HRTEM images of authigenic I–S and detrital illite at different depths show variable types of crystal-chemical features (Fig. 5a–c). The I–S mix-layered particles in the samples at 3,066 and 3,436 m show a high degree of variation in both shape and size. The crystallites are partly folded or kinked and contain different amounts of lattice defects, in particular layer terminations. These microstructures may form as growth defects in low temperature diagenetic environments or by the migration of defects associated with rock deformation. Although the precise origin in these samples is unclear, these microstructures are most abundant close to the main fault (3,436 m, Fig. 5a, b).

In addition to this variability, the thickness of clay particles can range from 2 to 50 nm, with lengths typically more than 100 nm. The I–S particles at 3,066 m in Fig. 5a are 2–10 nm thick, show straight crystallite boundaries and a relatively high degree of ordering. In comparison, the rocks at 3,436 m reveal slightly thicker I–S particles of 5–15 nm thickness, display irregular crystallite boundaries and a random arrangement of mixed-layers (Fig. 5b). In the deepest sample-set three, authigenic assemblages of illite ca. 10–30 nm in average thickness occurs adjacent to chlorite packets of similar thickness (Fig. 5c). Here, C–S crystallites were also detected with straight crystal boundaries and regularly ordered 1:1 alterations (corrensite based on XRD data). At this depth, I–S occurs only as

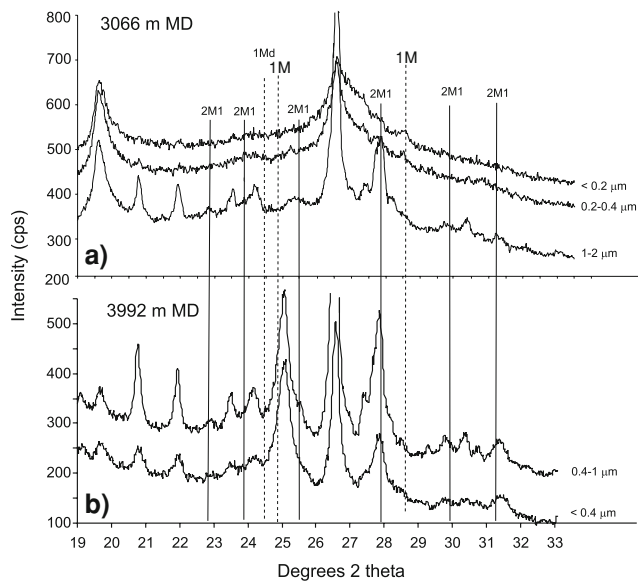


Fig. 4 Polytype determination at **a** 3,066 m and **b** 3,992 m, with a 1M/1Md polytype dominating the finer-grain sizes, and the 2M polytype reflecting the detrital mica in the larger-grain sizes

randomly ordered phases, but these are rarely observed in the TEM.

Quantitative mineral compositions of illitic minerals determined by analytical electron microscopy (AEM) are expressed as average structural formulae by normalizing to $\text{O}_{10}(\text{OH})_2$. The chemistry of the fine-grained authigenic crystallites at 3,066 and 3,435 m show distinct differences in both interlayer and octahedral composition (Fig. 5d; Table 2). The K content ranges from an illitic composition (~ 0.75 per unit formula = puf) to I–S with depleted interlayer values approaching 0.4 puf. The most K-enriched illite, with an average composition of $\text{K} \sim 0.75$ puf was recorded from the fine-grained shear zone at 3,066 m, with an average structural formula of $\text{K}_{0.75}(\text{Al}_{0.6}\text{Fe}_{0.4}\text{Mg}_{0.25})[\text{Si}_{3.4}\text{Al}_{0.6}]\text{O}_{10}(\text{OH})_2$. However, the most K-depleted illitic mineral was measured in the mudrock closest to the main fault at 3,436 m, with a typical composition of around $\text{K}_{0.40}(\text{Al}_{0.95}\text{Fe}_{0.25}\text{Mg}_{0.35})[\text{Si}_{3.05}\text{Al}_{0.95}]\text{O}_{10}(\text{OH})_2$. Although the structural formula of illite at 3,992 m was not determined by semiquantitative AEM analyses, these minerals indicate K-rich phases.

Figure 5d shows the variation in I–S and illite composition by plotting interlayer (K–Ca–Na) and octahedral (Mg–Fe) cation content against Si. The strongest degree of K depletion and variability is recognized in the fault at 3,436 m, ranging from 0.3 to 0.6 puf. Samples from 3,066 m differ in their interlayer content, ranging from K concentrations of 0.6–0.95 puf, which are closer to pure illite–muscovite compositions. The octahedral cation content (Mg–Fe) also shows notable differences between the shallow fault and the main fault samples with the lowest

content of octahedral cations recorded close to the main fault (3,436 m). Octahedral Al^{VI} is relatively consistent (1.25–1.35 puf), and as is the Mg content (0.25–0.35 puf) at 3,066 and 3,436 m depths. The Fe content on the other hand is lower in the main fault at 3,435 m with 0.25 puf compared to 0.4–0.5 puf for the sheared mudrocks located at 3,066 m.

X-ray diffraction characteristics of mixed-layered phases

All sample-sets differ in the occurrence and abundance of I–S and illite, as well as chlorite and C–S. There are also recognizable differences in the amount of smectite in the mixed-layered minerals. In Fig. 6a–c, the 001 and 002 chlorite peaks at 14.5 and 7 Å, and the 001 peak of illite and I–S at 10–13.8 Å are plotted in the air-dried and ethylene-glycol states. The diffraction pattern of the air-dried sample at 3,066 m (Fig. 6a) shows a broad peak with two maxima, caused by an overlapping 10-Å illite reflection and an 11-Å I–S peak. Treatment with ethylene glycol shifted the latter to 12 Å, which is characteristic of relatively small amounts of interlayer smectite and a relatively high degree of ordering (Moore and Reynolds 1997). The main fault (at 3,436 m) contains a chlorite phase with minor amounts of C–S, visible from the small shift toward higher d values after ethylene-glycol treatment and a decrease in the intensity of the 7 Å reflection. These mixed-layers were also visible by TEM, and are similar to minerals described in the exhumed Punchbowl fault rocks by Solum et al. (2003).

Based on the peak shape and peak position of I–S reflections, samples closer to the main fault (3,436 m) contain slightly larger amounts of smectite interlayers, as indicated by the relatively broad peak at 12.7 Å after ethylene glycol treatment. NEWMOD (Moore and Reynolds 1997) calculations indicate $\sim 80\%$ illite and $\sim 20\%$ smectite for sample-set 1 at 3,066 m, and $\sim 70\%$ illite and $\sim 30\%$ smectite for samples at 3,436 m (Table 1). The mudrocks at 3,992 m contain no detectable smectite interlayers in the XRD pattern, and NEWMOD calculations indicate $>98\%$ illite content (Table 1).

Water content

Thermal-gravimetric and differential thermal analyses show different amounts of water loss from the mudrock lithologies of the three sample locations (Fig. 7a–d; Table 1). Based on the whole-rock mineral assemblage of quartz, feldspar, mica and matrix clay minerals, the release of water can be largely attributed to the hydrous clays and, in particular, to the smectite content. The weight-loss curves indicate three distinct stages of water loss at

Fig. 5 HRTEM lattice fringe images at different depths including microchemical analysis (AEM; normalized to $O_{10}(OH)_2$) of the sheared mudrocks; **a** mudrock sample at 3,066 m show ordered I–S mixed-layers with straight crystallite boundaries and less deformation features, **b** at 3,436 m, the I–S crystals are randomly ordered, with irregular crystal boundaries and a higher amount of deformation features, **c** at 3,992 m, lower amounts of smectite interlayers and deformation features occur, **d** chemical analysis of the sheared mudrocks show a higher depletion of interlayer and octahedral cations within the sample at 3,436 m, reflecting a higher degree of higher fluid–rock interaction

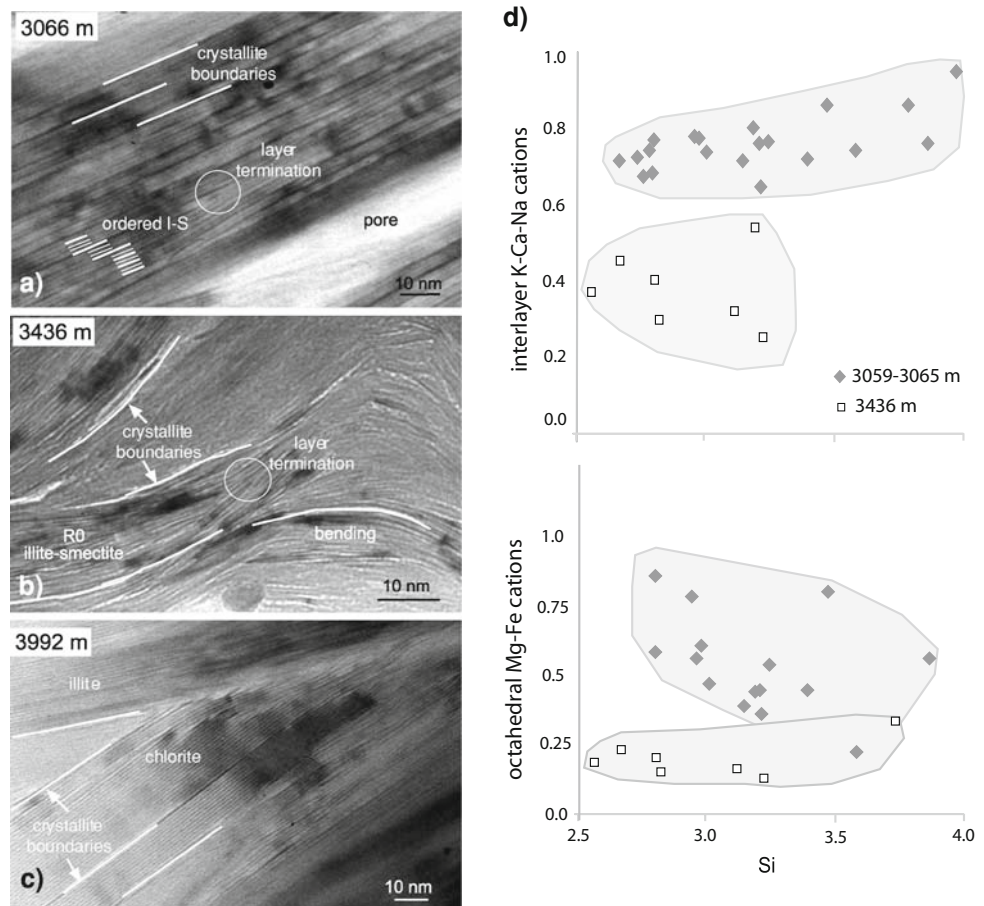


Table 2 Illite composition normalized to $O_{10}(OH)_2$ of two different mudrocks within the of the San Andreas Fault zone at 3,066 and 3,436 m

Illite composition normalized to $O_{10}(OH)_2$	Si	Al ^{iv}	Al ^{vi}	Mg	Fe	Σ oct	K	Na	Ca	Σ int
3,066 m	3.40	0.60	1.25	0.25	0.40	0.65	0.75	0.0	0.1	0.85
3,436 m	3.05	0.95	1.35	0.35	0.25	0.60	0.40	0.0	0.2	0.60

100–200°C, 400–650°C, and in some samples at about 980°C. The water-loss behavior from 50°C to about 240°C can be attributed to the hydration state of smectite layers in illite–smectite minerals, which is strongly influenced by the nature of interlayer cations, as well as by factors such as particle size and shape (Grim and Bradley 1948).

At 3,066 m, the initial stage of water loss appears at 90.8–380.4°C, which represents 0.65% weight loss due to the dehydration of smectite interlayers (Fig. 7a). The highest water loss can be recognized in the interval between 380 and 602°C, with 2.7% weight loss corresponding to the release of crystalline water during dehydroxylation of both I–S and illite. At >985°C, a weight loss of 0.31% occurred, which is attributed to further mineral breakdown at higher temperature and probably relates to a spinel phase transition. Overall, the total loss of weight due to volatile release is 3.7%.

At 3,436 m, the total weight loss during heating is higher by 6.5% (Fig. 7b). Water loss at low temperatures between 0 and 70°C causes 1.62% of weight loss, and is attributed to the loss of adsorbed surface water, whereas remaining interlayer water is removed between 70 and 109°C with 1.29% of weight loss. The total amount of interlayer water is estimated to be 2.96%. Most of the crystalline water was lost between 409 and 573°C, with 2.62% weight loss, and between 573 and 1,150°C, with 0.93% loss. The exothermic peak in the DTA profile at 900°C is again attributed to the crystallization of a spinel phase.

The least weight loss is found in the deepest sample at 3,992 m, with a total loss of 2.75% (Fig. 7c). Only minimal (<0.3%) interlayer water loss occurs at temperatures below 216°C, and a further ca. 1% between 216 and 460°C. The dehydroxylation of both illite and chlorite between 460 and 667°C corresponds to the largest weight loss of 1.65%,

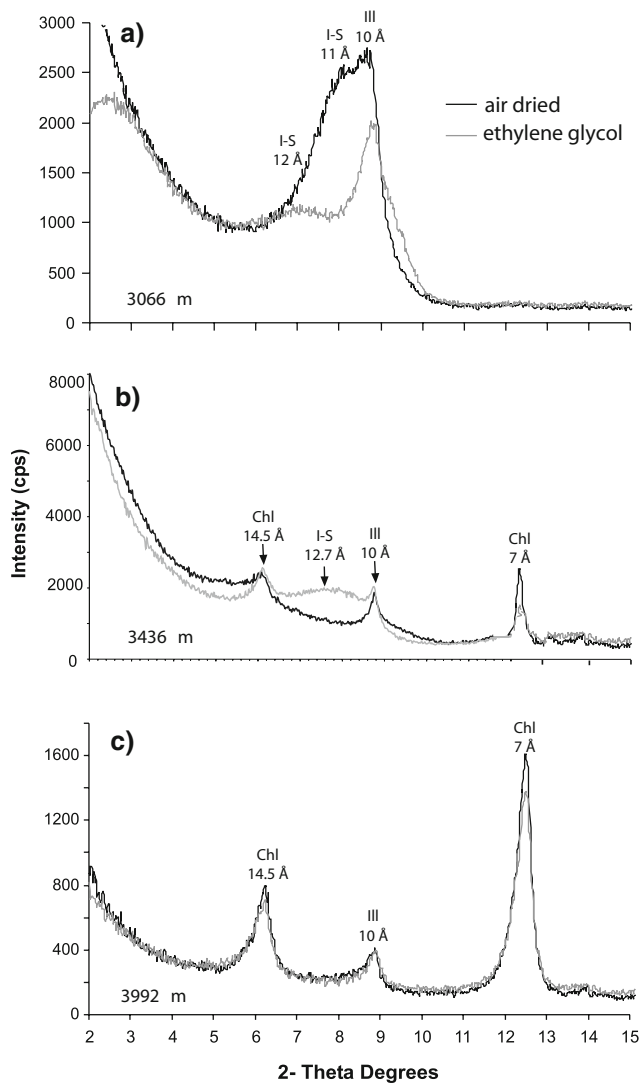


Fig. 6 X-ray diffraction patterns of clay minerals at **a** 3,066 m, **b** 3,436 m, and **c** 3,992 m depth. Air-dried and ethyl-glycolated texture (oriented) patterns. *Chl* chlorite, *I-S* illite–smectite, *Ill* illite

although volatile components are continually lost at a steady but slower rate up to 1,100°C.

The patterns of dehydration observed in the mudrock samples can be compared with the DTA pattern of Namontmorillonite drill mud that has been used during drilling operations (Fig. 7d). This uncontaminated sample shows the highest total weight loss of water of 10.5% (Fig. 7d). Here, 5.58% of adsorbed surface and interlayer water is lost between 0 and 88°C, 2.21% of water during further heating to 591°C, 2.19% up to 694°C and a final 0.49% up to 1,100°C.

Discussion

This study of SAFOD core material from Phase 2 drilling characterizes the origin and nature of diverse,

neomineralized fine-grained I–S and C–S phases that are present in the matrix of argillaceous, mudrock lithologies across the deep San Andreas Fault. These minerals occur in varying abundance, and their crystallization textures and composition do not conform to either a simple burial diagenetic pattern or one that can be solely attributed to the advective circulation of fluids during faulting.

All rock cuttings and core samples from the San Andreas Fault at depth show dominance in alteration features due to dissolution-precipitation reactions (see also Solum et al. 2006; Bradbury et al. 2007). The degree of cataclastic breakdown by repeated grain fracturing in these samples is only minor, but is most evident in sample sets 1 and 2. Both quartz and feldspar clasts have highly sutured, curvilinear grain boundaries that are attributed to intense dissolution rather than grain fracturing. There is also abundant evidence of clast alteration and the production of low temperature clay minerals that are concentrated in the rock matrix. Minerals such as I–S, illite, chlorite and C–S appear to have crystallized at the expense of detrital feldspar and mica grains, including the breakdown of both muscovite and biotite. A schematic reconstruction of the mineral textures and rock fabric is presented in Fig. 8.

Rock deformation features are evident mainly in the clasts of the mudrocks. This is best seen from deformed mica microstructures in the coarser detrital fraction, which show varying degrees of grain fracturing and folding. As expected, the intensity of fracturing and folding is highest in samples from the core of the fault (3,436 m and to a lesser extent at 3,066 m) compared to clay-rich lithologies lying beneath the fault (3,992 m MD). XTG analyses of mica grains within intact rock fragments reveal weak fabrics in general throughout all depths. The weak fabrics of fault gouge or strongly deformed mudrocks appear to be common in nature and have been observed also elsewhere (Yonghong et al. 2001; Solum et al. 2003). The poor degree of fabric development probably reflects the focusing of fluids along the fault, which may give rise to enhanced fluid pressures during fault motion and/or postslip authigenic clay growth within the rock matrix. In spite of its greater depth, the silty mudrock lithology at 3,992 m appears to have a slightly weaker fabric, which conforms to the less deformed state of this lithology. Similar types of compaction fabrics are also observed at 1.8 to ca. 4 km depth within progressively buried deepwater mudstones in the sedimentary basin of the Gulf of Mexico, reflecting an apparently limited extent of illitization, and thus recrystallization, to which these sedimentary rocks were subjected (Aplin et al. 2006).

Authigenic I–S and, at deeper depths, illite growth appears to have occurred heterogeneously with various crystal sizes, shapes and polytypes. At 3,066 and 3,436 m mixtures of detrital $2M_1$ and authigenic $1M$ and $1M_d$

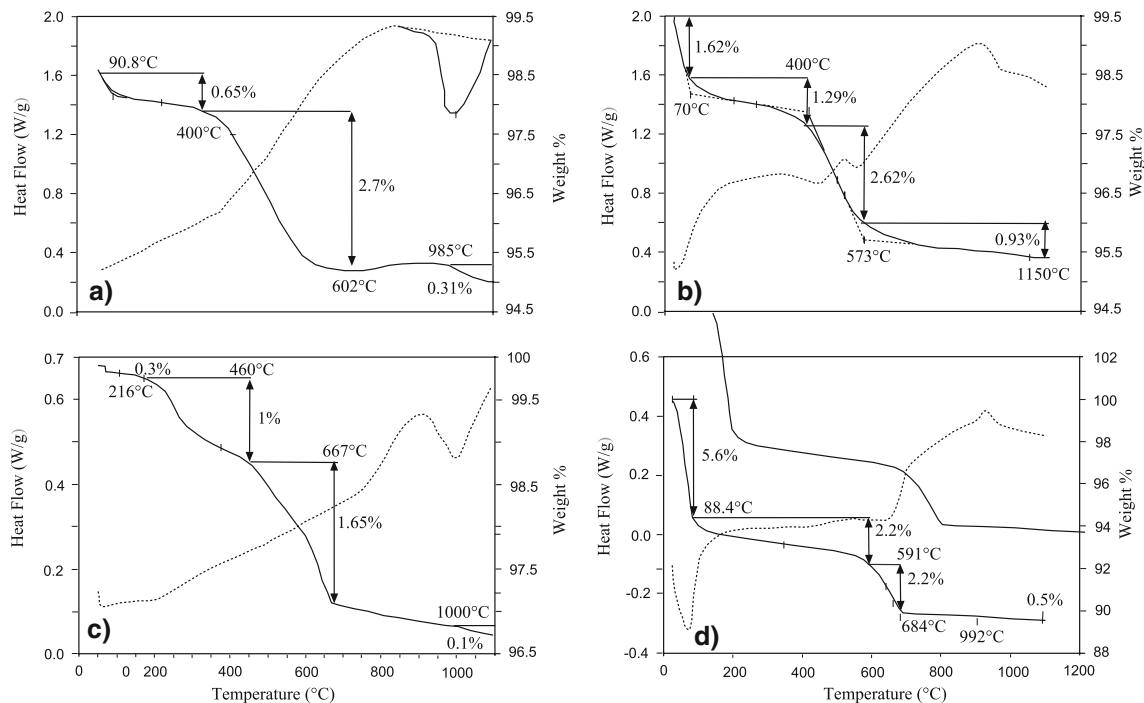


Fig. 7 Thermogravimetric (TGA, solid line) and differential thermal analysis (DTA, dashed line) plots showing different amounts of mineral-bound water in the three different sample locations, **a** at 3,066 m, total weight loss of 3.66%, **b** at 3,436 m, total weight loss of

6.5%, and **c** at 3,992 m, total weight loss of 2.75%. **d** presents the TGA and DTA pattern of the montmorillonite based drill mud used in the drilling operation. This unused mud sample has a total total weight loss of 10.5%

polytypes with pseudo-hexagonal shapes dominate these rocks, the latter mainly occurring as flaky crystallites coating the inside of open pores. The crystal-chemical features of the illitic minerals observed in relationship to vertical depth do not appear to conform to a simple burial diagenetic pattern where a progressive transformation from smectite to I-S and eventually pure illite is commonly observed with depth (Hunziker et al. 1986; Dong et al. 1997; Sachsenhofer et al. 1998). The sheared mudrock at 3,066 m contains an illite-rich (~80%) and an ordered I-S, whereas a few hundred meters deeper at 3,436 m a randomly ordered I-S (~70%) occurs. The deepest argillaceous lithology studied here at 3,992 m contains mainly authigenic illite and not more than 2–5% smectite interlayers.

I-S layer ratios have been widely used as an indicator of the degree of diagenetic alteration (Perry and Hower 1970), and since Hoffmann and Hower (1979) also as an empirical paleogeothermometer (an indicator of the maximum palaeotemperatures, Srodon et al. 2006; Table 1). Such temperature estimates can be made by comparison with illitization profiles from the shale lithologies of other sedimentary basin sequences. For example the degree of interlayered smectite (% smectite) in I-S minerals of the progressive burial diagenetic sequence in the East Slovak Basin is well defined (Sucha et al. 1993; Fig. 9) with a

transition from randomly ordered R0 to better ordered $R > 0$ occurring at ~110°C. The higher temperature transition to a well-ordered I-S mineral is often placed at ~170–180°C, based on the time-temperature model by Hoffmann and Hower (1979). Applying such relationships to SAFOD mudrocks, the I-S in the sample at 3,066 m (2,480 m TVD) indicates that a maximum paleotemperature of ~170°C was reached (Fig. 9). Similarly, the deepest sample-set at 3,992 m (3,014 m TVD) would indicate similarly high paleotemperatures of ~200°C. These temperatures imply a deeper diagenetic formation than today, or alternatively a higher paleogeothermal gradient of >5.0°C/100 m, and not the present ~3.5°C/100 m (Blythe et al. 2004). However, at 3,436 m (2,750 m TVD), the situation is different. Here, a paleotemperature lying between 170 and 200°C would be expected in a simple burial model but the amount of ~25% S in the I-S mixed-layers and the random ordering indicate a lower temperature of ~110°C, which is consistent with present thermal conditions (Fig. 9). One explanation for these differences could be the growth of new I-S minerals along the fault that are close to equilibrium with the current conditions at this depth. The increased amount of interlayer smectite in the I-S minerals may be related to the thin-film precipitations on fracture surfaces (Schleicher et al. 2006). In this scenario the more illite-rich varieties outside the main fault

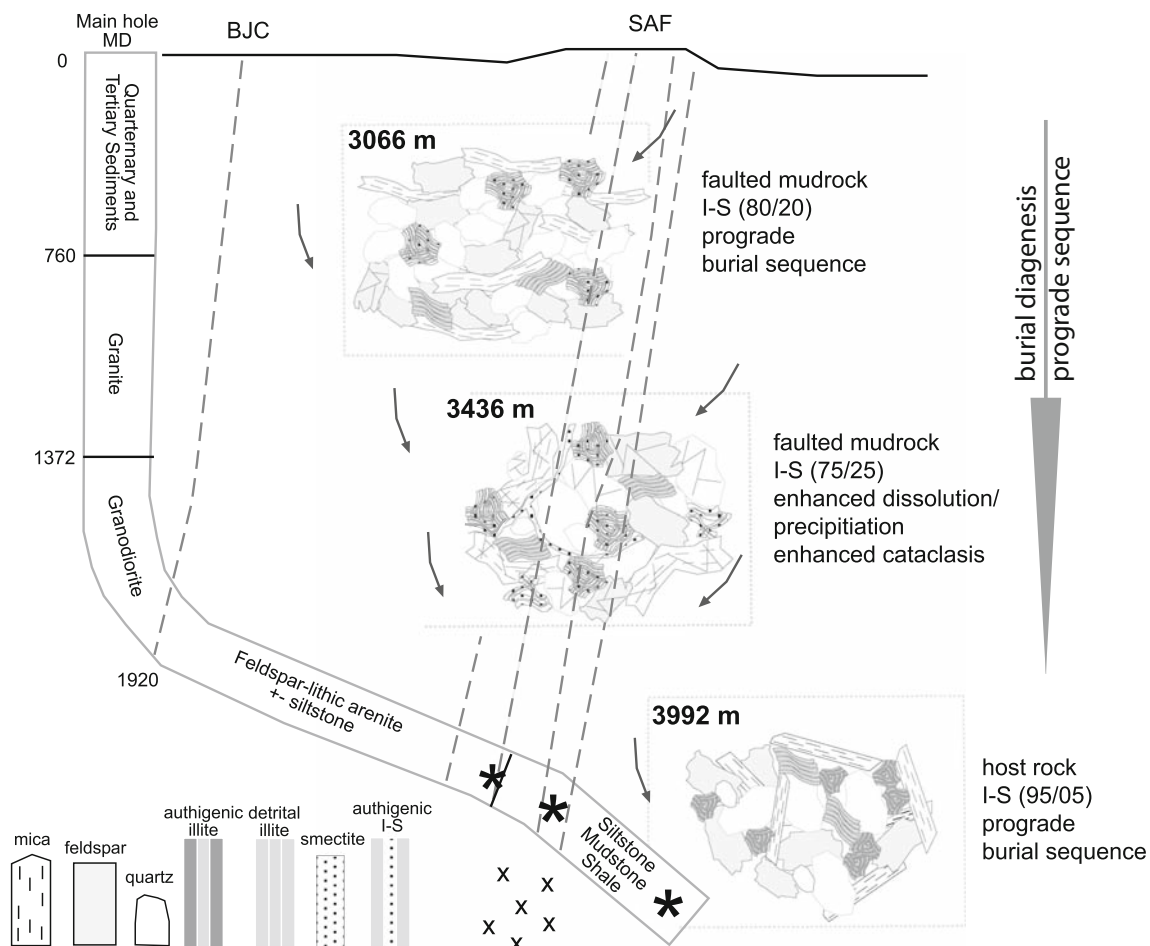


Fig. 8 Schematic model of the development of the minerals in the three sample-sets investigated, under the influence of burial diagenesis and faulting processes

are likely to represent older generations of diagenetic clay growth which formed either at deeper crustal depths before being partly exhumed, or were generated within a higher heat flow regime. However, one major uncertainty in applying the I–S geothermometer is that various kinetic factors influence reaction progress and therefore correlations between mixed-layer composition and the maximum burial temperature tend to be basin specific and apply to specific geothermal gradients and concentrations of K^+ in the aqueous fluid phase (Pollastro 1993).

Another more favorable approach that takes into account the main kinetic factors affecting the I–S reaction is the model by Huang et al. (1993). Despite the absence of a simple burial pattern in the SAFOD drillhole when plotting authigenic I–S minerals versus %-illite (in I–S), plotting the samples according to the relationships of Huang et al. (1993) implies that a large proportion of mixed-layered minerals in the mudrock matrix may have been formed by slow diagenetic reactions within a subsiding sedimentary basin sequence. The kinetic model shown in Fig. 10a

presents the case for a burial rate of 153 m/Ma and a K^+ concentration of 200 ppm for diagenetic fluids, which is applicable to the saline brines encountered in the SAFOD drillhole (Jim Thorsden personal communication). Two of the three samples that plot along the 3.5°C/m geothermal line (3,066 and 3,992 m) could have formed progressively during burial diagenesis as part of a continuous sequence of transformations starting from smectite at shallow depths and ending with pure illite at depth. Interestingly, the rapid decrease in smectite content at depths greater than 3,000 m, shown by the downturn in the curve, can explain the low abundance of smectite observed at 3,992 m.

Assuming a burial origin for I–S minerals and an initial smectite precursor, the kinetic model of Huang et al. (1993), which is based on experimental constraints, can also be applied to estimate the age of diagenesis. For an I–S with 80% illite layers, as detected in the upper part of the fault zone, a present-day borehole temperature of 112°C (Zoback et al. 2005; Williams et al. 2006) and an K^+ concentration of diagenetic fluids between 100 and

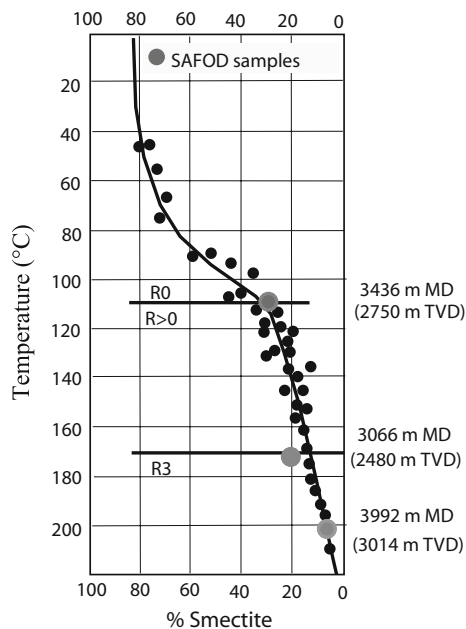


Fig. 9 Illitization profile modified after Sucha et al. (1993), based on the mudrock of the West Slovak Basin. This profile has been used to estimate the maximum palaeotemperatures attained for the SAFOD rocks based on the % of smectite (%S) recorded in I–S minerals. Gray dots reflect the SAFOD samples

200 ppm, the time required for this state of reaction progress is calculated to be in the range of 4–11 Ma (Fig. 10b). However, the sheared mudrock within the main fault contains more smectite than is predicted by the kinetic model. This randomly ordered I–S associated with notable fracturing and vein mineralization is attributed to fault-related precipitation and is likely related to the fracture coating mineral assemblages that was described by Schleicher et al. (2006).

The more water-rich mineral assemblages located along the main fault are prime candidates to explain the localized mechanical weakness of this plate boundary structure. The higher water content is not only related to the higher proportion of smectite phases in I–S minerals, but also to the occurrence of C–S mixed layered minerals in these samples. All these hydrous mineral phases can be considered to have formed during enhanced circulation of aqueous fluids along permeable fractures and veins by intense dissolution-precipitation reactions (Tourscher et al. 2008). There are a number of possibilities to explain the smectite content in the I–S of these fault-related precipitations. One likely reason is the local circulation of a larger volume of more diluted aqueous fluids that contain lower K^+ concentration than those of sedimentary brines. Such fluids may result from the down flow of meteoric waters into the crust, as documented in a number of crustal scale strike-slip faults zones (O’Neil 1985; Janssen et al. 1998, 2007). Other explanations may involve the infiltration of cooler fluids

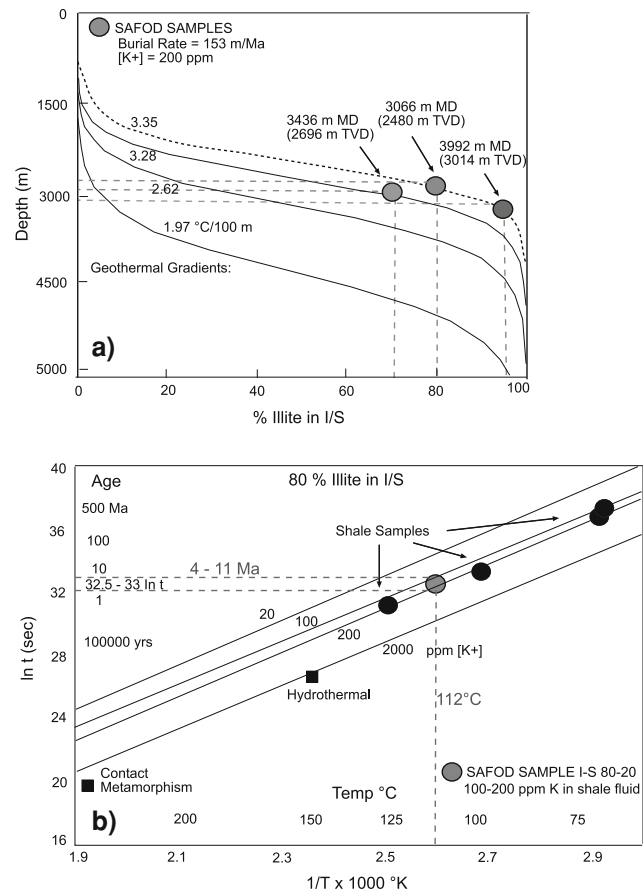


Fig. 10 **a** The kinetic model by Huang et al. (1993) presents the case for a burial rate of 153 m/Ma and a K^+ concentration of 200 ppm for the composition of diagenetic fluids. As two of the three samples plot along the 3.35°C/m geotherm indicates that these I–S minerals could have formed progressively during burial diagenesis as part of a continuous sequence of transformations starting from smectite at shallow depths and ending with pure illite at depth, **b** for I–S with 80% illite layers, as detected in the upper part of the fault zone, a present-day borehole temperature of 112°C and an K^+ concentration of diagenetic fluids between 100 and 200 ppm, the time required for this state of reaction progress can be calculated to be in the range of 4–11 Ma

into the fault zone during the multiple episodes of seismogenic faulting. Because it is evident that the precipitation of smectite interlayers offers an important fault-weakening mechanism, our current knowledge of the kinetics of mixed-layered clay growth in seismically active fault zones would benefit from continued study.

Acknowledgments The Deutsche Forschungsgemeinschaft (DFG Project SCHL 1821/1-1 and 1-2), and the National Science Foundation (EAR-0345985) provided support for our SAFOD research. The CGS at the University of Strasbourg is thanked for allowing us access to their laboratory equipment. Thanks to Steve Hickman and John Solum for providing samples and to our colleagues from the SAFOD project for discussions. Chris Marone and an anonymous reviewer are thanked for helpful comments and corrections that resulted in an improved presentation of the work.

References

- Aplin AC, Matenaar IF, Mc Carty DK, van der Pluijm BA (2006) Influence of mechanical compaction and clay mineral diagenesis on the microfabric and pore-scale properties of deep-water Gulf of Mexico mudstones. *Clays Clay Miner* 54(4):500–514. doi:10.1346/CCMN.2006.0540411
- Bird P (1984) Hydration-phase diagrams and friction of montmorillonite under laboratory and geologic conditions, with implications for shale compaction, slope stability and strength of fault gouge. *Tectonophysics* 107:235–260. doi:10.1016/0040-1951(84)90253-1
- Blythe AE, d'Alessio MA, Buegmann R (2004) Constraining the exhumation and burial history of the SAFOD pilot hole with apatite fission track and (U/Th)/He thermochronometry. *Geophys Res Lett* 31:L15S16. doi:10.1029/2003GL019407
- Boness NL, Zoback M (2006) Mapping stress and structurally controlled crustal shear velocity anisotropy in California. *Geology* 34(10):825–828. doi:10.1130/G22309.1
- Bradbury KK, Barton DC, Solum JG, Draper SD, Evans JP (2007) Mineralogic and textural analyses of drill cuttings from the San Andreas Fault Observatory at Depth (SAFOD) boreholes: initial interpretations of fault zone composition and constraints on geologic models. *Geosphere* 3(5):299–318. doi:10.1130/GES00076.1
- Day-Stürat RJ, Aplin AC, Srodon J, van der Pluijm BA (2008) Diagenetic reorientation of phyllosilicates minerals in paleogene mudstones of the Podhale basin, South Poland. *Clays Clay Miner* 56(1):100–111. doi:10.1346/CCMN.2008.0560109
- Dickinson WR (1966) Structural relationships of San Andreas fault system, Cholame Valley and Caslte Mountain Range, California. *Geol Soc Am Bull* 77:707–726. doi:10.1130/0016-7606(1966)77[707:SROSAF]2.0.CO;2
- Dong H, Peacor DR, Freed RL (1997) Phase relations among smectite, R1 illite-smectite and illite. *Am Mineral* 82:379–391
- Draper SD, Boness NL, Evans JP (2005) Source and Significance of the Sedimentary Rocks in the SAFOD Borehole: Preliminary Analysis. *Eos Trans AGU* 86(52):T24B–02
- Evans JP, Chester FM (1995) Fluid–rock interaction in faults of the San Andreas system: inferences from San Gabriel fault rock geochemistry and microstructures. *J Geophys Res* 100(B7):13007–13020. doi:10.1029/94JB02625
- Grim RE, Bradley WF (1948) Rehydration and dehydration of the clay minerals. *Am Mineral* 33:50–59
- Grim RE, Rowland RA (1944) Differential thermal analysis of clays and shales, control and prospecting method. *Am Ceram Soc J* 27:65–76. doi:10.1111/j.1151-2916.1944.tb14871.x
- Hansen PL, Lindgreen H (1989) Mixed layer illite/smectite diagenesis in Upper Jurassic claystones from the North Sea and onshore Denmark. *Clay Miner* 24(2):197–213. doi:10.1180/claymin.1989.024.2.07
- Hickman SH, Zoback MD, Ellsworth WL (2004) Introduction to special sections: preparing for the San Andreas Fault Observatory at Depth. *Geophys Res Lett* 31:L12S01. doi:10.1029/2004GL020688
- Hickman S, Zoback M, Ellsworth W (2005) Structure and composition of the San Andreas Fault Zone at Parkfield: results from SAFOD Phase 1 and 2, EOS 87 (Fall Meet. Suppl.), abstr. T23E-05
- Ho NC, Peacor DR, van der Pluijm BA (1999) Preferred orientation of phyllosilicates in Gulf Coast mudstones and relation to the smectite–illite transition. *Clays Clay Miner* 47:495–504. doi:10.1346/CCMN.1999.0470412
- Hoffmann J, Hower J (1979) Clay mineral assemblages as low grade metamorphic geothermometers: application to the thrust faulted disturbed belt of Montana, USA. *SEPM Spec Publ* 26:55–79
- Huang W, Longo JM, Pevear DR (1993) An experimentally derived kinetic model for smectite to illite conversion and its use as a geothermometer. *Clays Clay Miner* 41(2):162–177. doi:10.1346/CCMN.1993.0410205
- Hunziker JC, Frey M, Clayer N, Dallmeyer RD, Friedrichsen H, Flehming W et al (1986) The evolution of illite to muscovite: mineralogical and isotopic data from the Glarus Alps, Switzerland. *Contrib Mineral Petrol* 92:157–180. doi:10.1007/BF00375291
- Ikari MJ, Saffer DM, Marone C (2007) Effect of hydration state on the frictional properties of montmorillonite-based fault gouge. *J Geophys Res* 112:B06423. doi:10.1029/2006JB004748
- Janssen C, Laube N, Bau M, Gray DR (1998) Fluid regime in faulting deformation of the Waratah Fault Zone, Australia, as inferred from major and minor element analysis and stable isotopic signatures. *Tectonophysics* 294(1–2):109–130. doi:10.1016/S0040-1951(98)00127-9
- Janssen C, Romer RL, Plessen B, Naumann R, Hoffmann-Rothe A, Matar A (2007) Contrasting fluid regimes along the Dead Sea Transform. *Geofluids* 7:275–291. doi:10.1111/j.1468-8123.2007.00185.x
- Kim J, Peacor DR, Tessier D, Elsass F (1995) A technique for maintaining texture and permanent expansion of smectite interlayers for TEM observations. *Clays Clay Miner* 43:51–57. doi:10.1346/CCMN.1995.0430106
- Lanson B, Champion D (1991) The I/S-to-illite reaction in the late stage diagenesis. *Am J Sci* 291:473–506
- Moore DM, Reynolds RC (1997) X-ray diffraction and the identification and analysis of clay minerals. Oxford University Press, Oxford, p 378
- Moore DE, Rymer MJ (2007) Talc bearing serpentinite and the creeping section of the San Andreas fault. *Nature* 448(16):795–797. doi:10.1038/nature06064
- Morrow CA, Solum JG, Tembe SD, Lockner DA, Wong TF (2007) Using drill cutting separates to estimate the strength of narrow shear zones at SAFOD. *Geophys Res Lett* (submitted)
- Nadeau R, Michelini A, Uhrhammer R, Dolenc D, McEvelly T (2004) Fault structure, microearthquake recurrence and deep fault slip surrounding the SAFOD target. *Geophys Res Lett* 31:L12S08. doi:10.1029/2003GL019409
- Nieto F, Ortega-Huertas M, Peacor DR, Arostegui J (1996) Evolution of illite/smectite from early diagenesis through incipient metamorphism in sediments of the Basque-Cantabrian Basin. *Clays Clay Miner* 44(3):304–323. doi:10.1346/CCMN.1996.0440302
- O'Neil JR (1985) Water–rock interactions in fault gouge. *Pure Appl Geophys* 122:440–446. doi:10.1007/BF00874610
- Oertel G (1985) The relationship of strain and preferred orientation of phyllosilicate grains in rocks: a review. *Tectonophysics* 100:413–447. doi:10.1016/0040-1951(83)90197-X
- Page BM, Thompson GA, Coleman RG (1998) Late Cenozoic tectonics of the central and southern Coast Ranges of California. *Geol Soc Am Bull* 110:846–876. doi:10.1130/0016-7606(1998)110<0846:OLCTOT>2.3.CO;2
- Pares JM, Schleicher AM, van der Pluijm BA, Hickman SH (2008) Paleomagnetic reorientation of the SAFOD borehole. *Geophys Res Lett* 35:L02306. doi:10.1029/2007GL030921
- Peacor DR (1992) Diagenesis and low-grade metamorphism of shales and slates. In: Buseck PR (ed) *Minerals and reactions at atomic scale: transmission electron microscopy*, *Rev Mineral* 27:335–380
- Perry E, Hower J (1970) Burial diagenesis in Gulf Coast pelitic sediments. *Clays Clay Miner* 18:165–177. doi:10.1346/CCMN.1970.0180306
- Pollastro RM (1993) Consideration and applications of the illite/smectite geothermometer in hydrocarbon-bearing rocks of

- Miocene to Mississippian age. *Clays Clay Miner* 41(2):119–133. doi:[10.1346/CCMN.1993.0410202](https://doi.org/10.1346/CCMN.1993.0410202)
- Reynolds RC, Reynolds RC (1996) NEWMOD: a computer program for the calculation of one-dimensional diffraction patterns of mixed-layered clays. Hanover, New Hampshire
- Rutter EH, Maddock RH, Hall SH, White SH (1986) Comparative microstructure of natural and experimentally produced clay bearing fault gouges. *Pure Appl Geophys* 24:3–30. doi:[10.1007/BF00875717](https://doi.org/10.1007/BF00875717)
- Rutter EH, Holdsworth RE, Knipe RJ (2001) The nature and tectonic significance of fault-zone weakening: an introduction. *Geological Society of London. Spec Publ* 186(1):1–11
- Sachsenhofer RF, Rantitsch G, Hasenhuettl C, Russegger B, Jelen B (1998) Smectite to illite diagenesis in early Miocene sediments from the hyperthermal western Pannonian Basin. *Clay Miner* 33:523–537
- Saffer DM, Marone C (2003) Comparison of smectite- and illite-rich gouge frictional properties: application to the updip limit of the seismogenic zone along subduction megathrusts. *Earth Planet Sci Lett* 215:219–235. doi:[10.1016/S0012-821X\(03\)00424-2](https://doi.org/10.1016/S0012-821X(03)00424-2)
- Schleicher AM, van der Pluijm BA, Solum JG, Warr LN (2006) The origin and significance of clay minerals on surfaces, in fractures and in veins from SAFOD borehole samples (Parkfield, California). *Geophys Res Lett* 33:L16313
- Solum JG, van der Pluijm BA (2005) Phyllosilicate mineral assemblages of the SAFOD pilot hole and comparison with an exhumed segment of the San Andreas Fault system. *Geophys Res Lett* 31:L15S19. doi:[10.1029/2004GL019909](https://doi.org/10.1029/2004GL019909)
- Solum JG, van der Pluijm BA, Peacor DR, Warr LN (2003) Influence of phyllosilicate mineral assemblages, fabrics, and fluids on the behavior of the Punchbowl fault, southern California. *J Geophys Res* 108, B5: 5–1 to 5–12
- Solum JG, Hickman SH, Lockner DA, Moore DE, van der Pluijm BA, Schleicher AM et al (2006) Mineralogical characterization of protolith and fault rocks from the SAFOD main hole. *Geophys Res Lett* 33:L21314. doi:[10.1029/2006GL027285](https://doi.org/10.1029/2006GL027285)
- Srodon J, Morgan DJ, Eslinger EV, Eberl DD, Karlinger MR (1986) Chemistry of illite/smectite and end-member illite. *Clays Clay Miner* 34(4):368–378. doi:[10.1346/CCMN.1986.0340403](https://doi.org/10.1346/CCMN.1986.0340403)
- Srodon J, Kotarba M, Biron A, Such P, Clauer N, Wojtowicz A (2006) Diagenetic history of the Podhale-Orava Basin and the underlying Tatra sedimentary structural units (Western Carpathians): evidence from XRD and K-Ar of illite-smectite. *Clay Miner* 41:751–774. doi:[10.1180/0009855064130217](https://doi.org/10.1180/0009855064130217)
- Sucha V, Kraus I, Gerthofferova H, Petes J, Serekova M (1993) Smectite to illite conversion in bentonites and shales of the East Slovak Basin. *Clay Miner* 28:243–253. doi:[10.1180/claymin.1993.028.2.06](https://doi.org/10.1180/claymin.1993.028.2.06)
- Tembe SD, Lockner DA, Solum JG, Morrow CA, Wong TF, Moore DE (2006) Frictional strength of cuttings and core from SAFOD drillhole phases 1 and 2. *Geophys Res Lett* 33:L23307. doi:[10.1029/2006GL027626](https://doi.org/10.1029/2006GL027626)
- Thurber C, Roecker S, Zhang H, Baher S, Ellsworth WL (2004) Fine-scale structure of the San Andreas fault zone and location of the SAFOD target earthquakes. *Geophys Res Lett* 31:L12S02
- Tourscher S, Schleicher AM, van der Pluijm BA, Warr LN (2008) Constraints on mineralization, fluid-rock interaction and mass transfer during faulting at 3 km depth from the SAFOD drill hole. *J Geophys Res* (submitted)
- van der Pluijm BA, Ho N-C, Peacor DR (1994) High-resolution X-ray texture goniometry. *J Struct Geol* 16:1029–1032. doi:[10.1016/0191-8141\(94\)90084-1](https://doi.org/10.1016/0191-8141(94)90084-1)
- Vrolijk P, van der Pluijm BA (1999) Clay gouge. *J Struct Geol* 21:1039–1048. doi:[10.1016/S0191-8141\(99\)00103-0](https://doi.org/10.1016/S0191-8141(99)00103-0)
- Wallace (ed) (1990) The San Andreas Fault System, California, Geological Survey, Professional Paper 1515, United States Government Printing Office, Washington
- Warr LN, Cox S (2001) Clay mineral transformation and weakening mechanisms along the Trans Alpine Fault, New Zealand, Geological Society London. *Spec Publ* 186:85–101
- Warr LN, Nieto F (1998) Crystallite thickness and defect density of phyllosilicates in low-temperature metamorphic pelites: a TEM and XRD study of clay mineral crystallinity index standards. *Can Mineral* 36:1453–1474
- Wenk HR (1985) Preferred orientation in deformed rocks (eds.), Academic Press, Orlando
- Williams CF, Grubb FV, Galanis SP Jr (2004) Heat flow in the SAFOD pilot hole and implications for the strength of the San Andreas Fault. *Geophys Res Lett* 31:L15S14. doi:[10.1029/2003GL019352](https://doi.org/10.1029/2003GL019352)
- Williams CF, Grubb FV, Galanis SP (2006) Heat-flow measurements across the San Andreas Fault near Parkfield, California, preliminary results from SAFOD. *EOS* 87 (Fall Meet. Suppl.), abstr. S33B-0241
- Wu FT, Blatter L, Roberson H (1974) Clay gouges in the San Andreas fault system and their possible implications. *Pure Appl Geophys* 113:87–96. doi:[10.1007/BF01592901](https://doi.org/10.1007/BF01592901)
- Yonghong Y, van der Pluijm BA, Peacor DR (2001) Deformation microfabrics of clay gouge, Lewis Thrust, Canada: a case for fault weakening from clay transformation. *Geological Society. Spec Publ* 186:103–112
- Zoback M, Hickman S, Ellsworth W (2005) Drilling, sampling and measurements in the San Andreas Fault Zone at seismogenic depth, *EOS* 87 (Fall Meet. Suppl.), abstr. T23E-01